A HIGH-PERFORMANCE DIPOLE SURFACE DRIVE FOR LARGE TRAVEL AND FORCE

Storrs Hoen, Qing Bai, Jonah A. Harley, David A. Horsley, Farid Matta, Tracy Verhoeven, Judy Williams, and Kirt R. Williams

Agilent Laboratories
3500 Deer Creek Road, Palo Alto, CA 94304 email: storrs_hoen@agilent.com

ABSTRACT

We report unparalleled travel, force, precision and repeatability with an electrostatically actuated dipole surface drive. We have successfully demonstrated motors that generate several hundred micronewtons while traveling 50 microns at 60 V. Without external feedback control, the motors can be positioned with nanometer resolution and repeatability. The manufacture of these motors uses a two-level polysilicon deposition, a wafer bond and two anisotropic deep silicon etches.

INTRODUCTION

An increasing variety of applications require large travel MEMS actuators with excellent precision and rapid positioning. Examples are miniature tunable lasers [1], low-cost portable imaging systems for scanning probe microscopes [2-5], optical data storage applications [6], and actuators for tilting mirrors [7, 8]. A variety of actuators have been proposed to satisfy the requirements of these applications. Most notably, Grade *et al*. [6] have produced a single axis electrostatic comb drive that traverses 200 µm in less than 1 ms at 150 V. Rodgers *et al*. [9] have developed a compact comb drive that generates 1.5 mN/mm^2 at 100 V. It has a range of motion of several microns. These actuators provide excellent performance. However, micromotors are required that can carry substantial loads and develop greater forces at reasonable drive voltages.

We previously reported a proof-of-concept electrostatic surface drive that operated as a stepper motor and achieved excellent conversion of applied voltage to applied force [10]. In that device, flexure width and thickness were not well controlled and the motor was assembled from individual stator and translator dies. Furthermore, when a bias voltage of more than 10 V was applied to the chrome motor electrodes in air, water would condense onto the electrodes and cause them to dissolve. This effect was most likely due to the large electrostatic fields and field gradients present in the dipole motor. For these reasons, that first motor was unsuitable for manufacture and incapable of providing either large force or large travel.

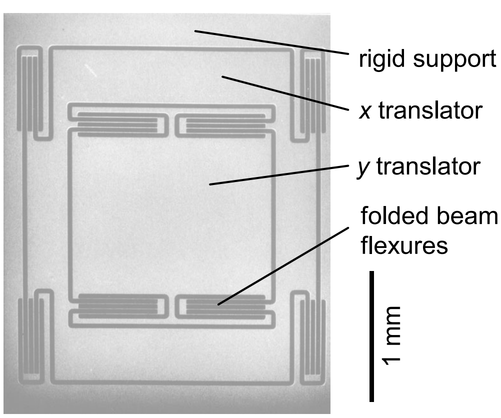

Figure 1. Scanning electron micrograph of the top surface of the translator. The central x-y *stage is 1.2 × 1.2 mm^2.*

BASIC DESCRIPTION AND METHOD OF OPERATION

In this paper, we describe the theory and method of operation, the manufacturing process, and the characteristic performance of the dipole stepper motor. A variety of flexure designs have been tested. A top view of a typical assembled motor is shown in Figure 1. The upper surface of the 100-µm-thick translator is smooth and flat, making it ideal for the mounting of other objects such as mirrors, gratings, and scanning probe samples. The motor is configured so that the x translator is attached to a rigid frame by 2.5-µm-wide folded beam flexures. The y translator is similarly attached to the x translator. The driving forces for these translators arise from the interactions between fringing fields created on the surfaces of both the translator and the stator. To achieve these fields, long strip electrodes oriented along the y and x directions are formed along the x and y translators, respectively. As shown in Figure 2, similarly oriented electrodes are formed on the stator surface. The flexures support the translator over the stator surface and allow it to move in the x-y plane relative to the stator.

The electrostatic model describing the operation of this motor has been developed in detail elsewhere [10]. We configure the electrodes on the bottom of the translator so

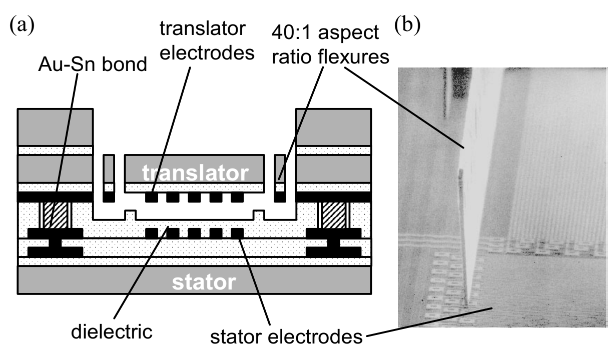

Figure 2. (a) Schematic cross-section of the dipole stepper motor. The gap between the translator and stator is approximately 2.5 microns. (b) SEM of the dipole motor after the translator has been removed showing one of the several flexures that support the translator over the stator electrodes.

0-7803-7731-1/03/$17.00

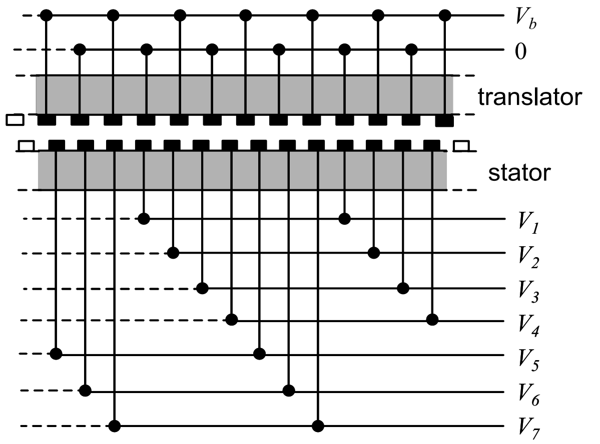

Figure 3. Schematic wiring diagram of the translator and stator electrodes. The translator electrodes alternate between V_b *and ground while a seven phase voltage pattern described in Table 1 is applied to the stator electrodes.*

that every other electrode is at the bias voltage while alternate electrodes are held at ground. This dipole voltage pattern is shown in Figure 3. The stator electrodes are arranged so that each is electrically connected to the electrode 7 electrodes away. Moreover, the stator pitch is chosen so that for every 6 translator electrodes there are 7 stator electrodes. For the particular motors described in this paper, the translator electrode pitch p_t and the stator electrode pitch p_s are 2.8 μm and 2.4 μm, respectively. A voltage pattern such as Pattern A in Table 1 is applied to the stator electrodes so that a spatially alternating voltage pattern is generated on its surface. The interaction of the two spatially alternating patterns on the translator and stator surfaces creates a sinusoidal potential. In the absence of external forces, the translator rests at the potential minimum where the force curve crosses zero with negative slope in Figure 4.

To move the translator, the voltage on one stator electrode is changed from V_b to ground or vice versa. Table 1 shows an example of this method in which Pattern A is changed to Pattern B and then to Pattern C by changing the voltage on one electrode at a time. This causes the electrical potential to be shifted in steps of $p_t/7$ or 0.4 μm. The translator rest position is similarly shifted by 0.4 μm. Importantly, the voltages applied to the *translator* electrodes are not altered when the motor is moved. If pattern of changing the voltage on one stator electrode by increments of V_b is continued for a total of 14 steps, the

Table 1. Voltage patterns applied to the electrodes shown in Figure 3.

	Stator Electrode Voltage						
	V_1	V_2	V_3	V_4	V_5	V_6	V_7
Pattern A	0	V_b	0	V_b	V_b	0	V_b
Pattern B	0	V_b	0	0	V_b	0	V_b
Pattern C	0	V_b	V_b	0	V_b	0	V_b
Pattern D	0	$0.9V_b$	V_b	0	V_b	0	V_b

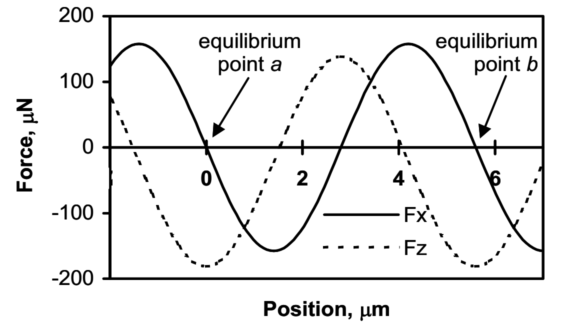

Figure 4. Lateral force (F_x) and out-of-plane force (F_z) calculated as functions of translator position for a bias voltage of 40V, a gap of 2.4 μm, a motor area of 1.84 mm^2 and a translator pitch of 2.8 μm.

original voltage pattern, Pattern A, is recovered and the motor will have moved from equilibrium point *a* to equilibrium point *b* in Figure 4.

To move the motor in increments of less than the 400 nm basic step size, the voltage on one electrode can be changed by a fraction of V_b. The linearity of the potential and translator positions with respect to the voltage applied this electrode to better than 1 part in 300. An example of this "microstepping" is shown in Table 1 and Figure 8. Changing from pattern C to Pattern D shifts the rest position of the motor $0.1p_t/7$ or 40 nm. A rudimentary 8-bit DAC provides a resolution of better than 1.5 nm.

FABRICATION

The stator is first formed as shown in Figure 5(a) using a two-level doped polysilicon process in which the stator electrodes and associated interconnects are patterned. A 2.5 μm thick oxide layer is then deposited. As shown in Figure 5(b), this dielectric is patterned in two levels with the highest level of the dielectric forming standoffs that set the height between the translator and stator. The lower dielectric level forms bumpers that ensure that, even during snap-in, shorting between the translator and stator electrodes is prevented. The final processing step for the stator, Figure 5(c), is to electroplate 2.5 μm of Au followed by 1.2 μm Sn.

The initial translator wafer, Figure 5(d), consists of single-level doped polysilicon on a silicon-on-insulator (SOI) wafer with a 100-μm-thick device layer and 380-μm-thick handle wafer. Flexures with a 40:1 aspect ratio are then formed, as shown in Figure 5(e) using the Bosch process in an STS ASE etcher. The large aspect ratio is required because there is substantial attractive force between the translator and stator as shown in Figure 4. Though the target width is 2.5 μm, variations in photolithography and the etch process causes the actual flexure thickness to range from 1.0 μm to 2.5 μm. A stop-on-oxide process is used to ensure that the flexures are not undercut when the etch terminates on the oxide underneath the device layer.

As shown in Figure 5(f), the translator is released by a deep silicon etch of the handle wafer followed by a vapor HF etch of the silicon oxide. The completed stator and translator wafers are bonded together at 320°C using a Au-

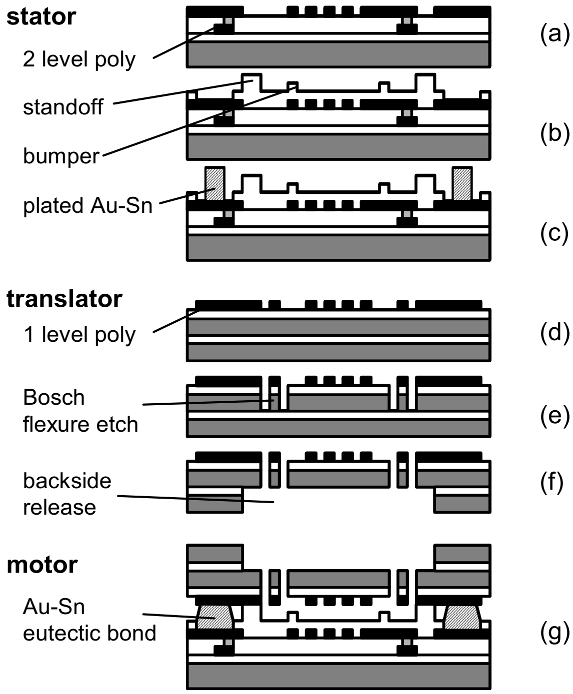

Figure 5. Abbreviated fabrication process for the dipole motor. The process steps for the stator and translator wafers are described in (a-c) and (d-f), respectively. The full motor is formed by wafer-scale bonding of the stator and translator wafers.

Sn eutectic bond. This bond both supports the translator over the stator and provides electrical connection between the two wafers. Because the translators are recessed from the back surface of the translator, the devices may be protected during singulation by placing dicing tape over the backside of the translator.

RESULTS AND DISCUSSION

The dipole stepping motor design allows these devices to provide large forces while traveling long distances along two directions. Figure 6 shows the characterization of a device with particularly narrow flexures. With no applied voltage, the rest position of the translator is determined by the equilibrium position of the flexures. As the bias voltage is increased from 0 V, the electrostatic potential soon dominates the mechanical potential of the flexures and the translator moves slightly to position itself at the equilibrium point of the electrostatic force curve as shown in Figure 4. Continuing to increase the bias voltage causes no further translation. Referring to Figure 4, the amplitude of the sinusoidal force curve increases but the position of the zero crossing does not change and thus the motor remains “locked” in its rest position.

To move the motor, the electrode voltages must be stepped as described in Table 1. This shifts the potential well and moves the translator. The flexures restrain the translator however, causing the motor to ride up the force curve. Shifting the voltage pattern continues to move the translator until the spring force is larger than the maximum electrostatic force $F_{x,max}$. At this point, maximum displacement for this particular bias voltage is reached and the motor snaps into a potential well that is closer to the origin. We denote the sum of the maximum translator displacements in negative and positive directions as the motor travel. The motor travel as a function of bias voltage is plotted in Figure 6. The travel increases at larger bias voltages until the motor contacts hard stops at ±25 µm. For this device with thin flexures, this occurs at a bias voltage of 18V.

With no applied voltage, the lateral resonant frequency is 127 Hz. As shown by Horsley *et al*. [11], this resonant frequency can be used to calculate the spring constant and effective thickness of the flexures. Since the translator has uniform thickness, its mass m can be calculated as 0.765 mg directly from its area and thickness. This implies that the spring constant of the flexures k_f is 0.49 N/m and the effective thickness is 1.0 µm.

In contrast to other electrostatic actuators, the lateral resonant frequency depends approximately linearly on the applied voltage. This effect is clearly seen in Figure 6 where the resonant frequency increases from 127 Hz to 1.6 kHz – more than a 10× improvement – as the bias voltage is increased from 0 – 30 V. This increase occurs because the resonant frequency f_0 depends on both the spring constant of the flexures k_f and the spring constant of the

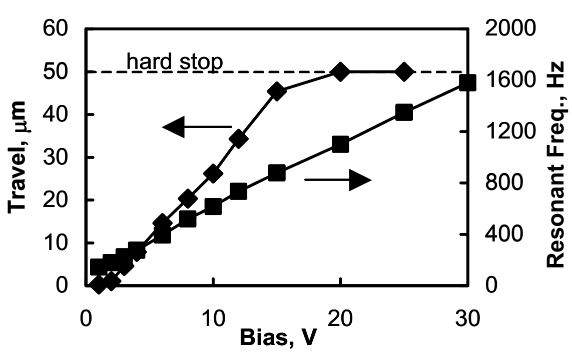

Figure 6. Measured motor travel and resonant frequency as functions of the applied bias for the x*-axis of a two axis motor. At bias voltages over 18V, the motor reaches hard stops at ±25 um.*

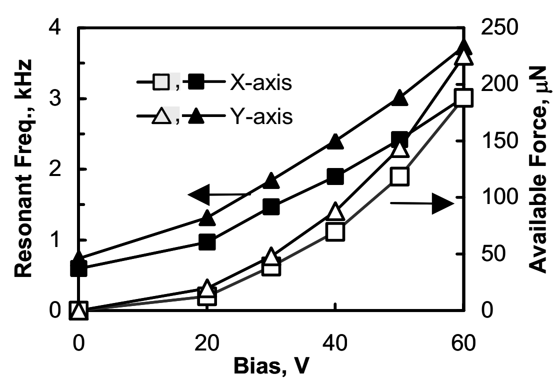

Figure 7. Measured resonant frequency and available force plotted as functions of the applied bias voltage for two axes of motion. The flexure width for this motor is 2.4 um.

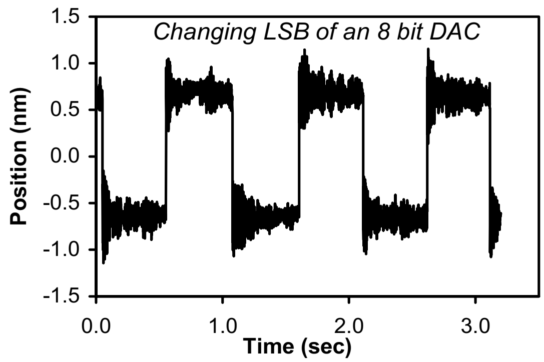

Figure 8. Measured motor position as the voltage on one of the seven independent stator electrodes is changed by 1/256th of the bias voltage. The voltage toggles every 0.5 seconds.

electrostatic potential k_{es}. In particular, f_0 can be expressed as:

$$f_0 = \left(\frac{1}{2\pi}\right)\sqrt{\left(k_{es} + k_f\right)/m} \; . \qquad (1)$$

The electrostatic spring constant k_{es} is the slope of the force curve at the motor position. If the translator position is near the equilibrium point, $k_{es} = (\pi/p_t)F_{x,max}$. Since the analytical model of the motor [10] predicts that $F_{x,max}$ grows as V_b^2, f_0 depends linearly on V_b in the range that $k_{es} > k_f$.

Figure 7 shows the resonant frequency and available force for *x* and *y* directions of a motor with 2.4-µm-wide flexures. This motor has a smaller *x* axis stage than the motor shown in Figure 1 and thus f_0 for the *x* axis is only slightly smaller (~10%) than that for the *y* axis at zero V_b. As expected from Eq. (1), the resonant frequency increases linearly with V_b for voltages at which $k_{es} > k_f$. There is very little damping of the motors in-plane and the Q measured for these resonances is ~200. Any vibration normal to the surface is strongly damped by squeeze film damping. The available force is calculated by inserting the resonant frequency in Eq. (1). We find that this motor can generate ~200 µN in both axes. The *x* and *y* forces are slightly different because the *y* electrode area is slightly larger than the *x* electrode area.

The electrical model [10] and the motor data can be used to calculate an effective electrical gap for these motors. The data of Figures 6 and 7 predict effective electrical gaps of 3.3 µm and 3.6 µm, respectively, although mechanical and

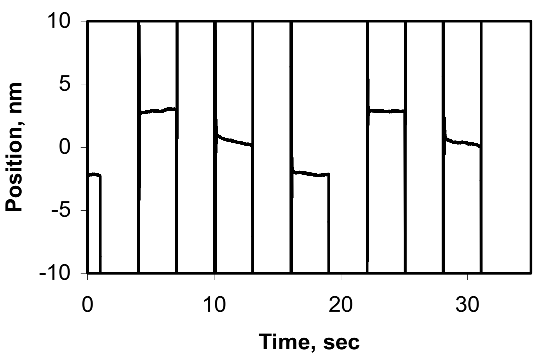

Figure 9. Motor position as a function of time as the motor is returned to the origin after various excursions. The position is changed every 3 sec.

SEM measurements confirmed a gap of ~2.6 µm.

The resolution inherent in the motor design is exhibited in Figure 8. A tilting mirror was attached to the motor to measure its position. As the applied voltage was changed by 1/256th of the bias voltage, the motor repeatably moves 1.5 nm. The measurement noise of ~0.3 nm arises from ambient vibrations in the tilting mirror. Using this same experimental setup, the open-loop position accuracy is plotted in Figure 9. The motor position is shown as a function of time as the motor returns to zero from positions 3, 5, and 10 µm away in both directions. The motor returns to the same position within 4 nm. The small offset is mostly due to some charging of the dielectric between the electrodes. For stability on longer time scales (~days), we found it necessary to control the ambient environment of the motor by enclosing it in a N_2 atmosphere.

CONCLUSIONS

We have demonstrated an electrostatic dipole stepping motor that provides large force and long travel. At a 60 V bias, it moves 50 µm and generates 200 µN. Moreover, it exhibits an open loop accuracy of ~ 4 nm. This actuator will be important for enabling a variety of positioning applications.

Acknowledgments

The authors thank J. Theil, M. Mottura, M. Ferrera and P. Ferrari for informative discussions and good advice.

References

[1] Jill D. Berger, *et al.*, "Widely tunable external cavity diode laser based on a MEMS electrostatic rotary actuator," *Proc. Optical Fiber Communication Conf.*, Anaheim, CA, TuJ1-TuJ4.

[2] easyScan Brochure, *Nanosurf AG,* Liestal, Switzerland. 2003.

[3] H. Rothuizen, *et al.*, "Fabrication of a micromachined magnetic x/y/z scanner for parallel scanning probe applications," *Microelect. Eng.* **53** 509-512 (2000).

[4] J.-J. Choi, *et al.*, "Electromagnetic micro x-y stage with very thick Cu coil for probe-based mass data storage device," *J. Semiconductor Technol. Sci.* **1** 84 (2001).

[5] P. Vettiger, *et al.*, "The "Millipede" - Nanotechnology entering data storage," *IEEE Trans. on Nanotech.* **1** 39-55 (2002).

[6] J.D. Grade, H. Jerman, and T.W. Kenny, "A large-deflection electrostatic actuator for optical switching applications," *Proc. Solid-State Sensor and Actuator Workshop*, Hilton Head, S.C. June 4-8, 2000 pp. 97-100.

[7] S. Hoen, "Optical cross-connect switch using electrostatic surface actuators," US 6,215,222 (1999).

[8] S.L. Miller, *et al.*, "Microelectromechanical apparatus for elevating and tilting a platform," WO 01/77001 (2001).

[9] M.S. Rodgers, *et al.*, "A new class of high force, low-voltage, compliant actuation systems," *Proc. Solid-State Sensor and Actuator Workshop*, Hilton Head, SC pp. 210-213.

[10] S. Hoen, *et al.*, "Electrostatic surface drives: theoretical considerations and fabrication," *Proc. 1997 Int. Conf. on Solid-State Sensors and Actuators*, Chicago. June, 1997 pp. 41-44.

[11] D.A. Horsley, *et al.*, "Multi-degree of freedom dynamic characterization of deep-etched silicon suspensions," *Proc. Solid-State Sensor and Actuator Workshop*, Hilton Head, SC. June 4-8, 2000 pp. 81-84.